

Instituto Tecnológico y de Estudios Superiores de Monterrey

Campus Monterrey

School of Engineering and Sciences



Auxiliary method based on effective medium theory for biosensing applications using surface plasmon resonance

A thesis presented by

Alejandro Balderas Elizalde

Submitted to the
School of Engineering and Sciences
in partial fulfillment of the requirements for the degree of

Master of Science

in

Nanotechnology

Monterrey, Nuevo León, May, 2020

Dedication

This thesis is dedicated to my family, who has always stood by my side and have made all of this possible.

Acknowledgements

I would like to express my deepest gratitude to all those who have been by my side in this journey and have made this thesis possible.

I am very grateful to my thesis advisor Dr. Raúl Hernández Aranda for being the one who motivated me to enter the Master's degree, for his friendship and his very valuable advice during these two years. I am also grateful to my co-advisor Dr. Gesuri Morales Luna for his help in the construction of the SPR biosensor and for helping me guide my thesis to its final result. I am very grateful to Marcela and Raúl for all those afternoons obtaining measurements from the microfluidic sensor and their help in understanding the functionalization of the layers.

I am very grateful to the people in the physics department: Adad, Luis Garza, Benjamin and Rafael; who have for always having a helpful disposition and being always available for the discussion of ideas. For their constant help, friendship and support that made these two more years more productive and enjoyable. I am also thankful for my friends Adriana and Rohan who were a fundamental part in the completion of this document by providing both academic and personal support, always making sure I took care of other parts of my life besides the academic one. I reiterate my thanks to my family who have always provided me with love and opportunities to help me grow and improve myself. Finally, I thank all the people whose names might not be written here but helped me complete this document one way or another.

A special thanks to Tecnológico de Monterrey for giving me a scholarship that allowed me to study this degree and to CONAcYT for their scholarship that helped pay for my living during this time.

Auxiliary method based on effective medium theory for biosensing applications using surface plasmon resonance

by

Alejandro Balderas Elizalde

Abstract

In this thesis, an auxiliary method based on the effective medium theory is applied to surface plasmon resonance (SPR) biosensing in order to extract quantitative properties of the biosensor functionalization. An automatized SPR biosensor array was built to perform intensity measurements in an automatized and controlled manner. Five gold layers with different Bovine Serum Albumin (BSA) deposition times were measured in the sensor and the refractive index and thickness of the sample were both estimated using the Gradient Descent method in combination of a theoretical model. These parameters were then introduced into two distinct effective medium theories in order to change a qualitative description of the surface coverage into a quantitative one. Yielding values of 30 % for the linear effective field approximation (EFA) and 50 % for the non-linear Quasicrystalline Approximation (QCA). Finally, a qualitative detection of a BSA-Carbamazapine (CBZ) was done utilizing the sensor in which there is a significant difference in the response of the sensor compared to the one of bare gold and BSA.

List of Figures

2.1	Schematic of a 2 layer system. The interface is located at $z = 0$ and both media are large enough to be considered infinite.	7
2.2	Dispersion relations including the plasmon propagation constant. a) For the two layer system the light line and the propagation constant can be identified yet they only cross at the bulk plasmon resonance ($y = 1$). b) For the 3-layer system the light lines may cross at points other than the bulk plasmon resonance, this intersection allows for the coupling of light and generation of the Surface Plasmon Resonance.	10
2.3	A 3 layer system (also known as the Kretschmann configuration) made of a BK7 prism, a gold layer of thickness d and an infinite outer medium of air. Given this system and the dispersion relation in 2.2b any light incident from the BK7 prism will generate a plasmon mode in the Air-Gold interface. . . .	10
2.4	Visualization of a system where the TMM can be applied; the fields on the left side correspond to the incident E_i and reflected E_r fields while the field on the right hand side is the transmitted field E_t . Each of the finite layers is characterized by a thickness d_i and refractive index n_i	11
2.5	Simulations of IMI structures taking into account variations of the gold and last insulator. a) The gold's thickness is varied. At thicknesses below 25nm the phenomena approaches the behavior of total internal reflection while at thicknesses above 75 the plasmonic response is minimized as the bulk behaviour is achieved. b) The output refractive index is varied. Changes in the refractive index cause a shift in the SPR angle yet as the refractive index approaches that of BK7 the plasmonic response disappears.	14
2.6	Simulations of IMII structures taking into account variations of the third layer's properties. a) Variations of the layer's thickness with a fixed refractive index shows that despite a large thickness of 100nm the plasmonic response isn't diminished. b) Variations of the refractive index with a fixed thickness show that the IMII system has a wider dynamic range while being able to detect a refractive index of 1.8 RIU.	15
3.1	Simulation of permittivity components according to EFA, both components showing a linear behaviour with respect to f . As f approaches one: a) The real permittivity converges to $3\gamma + 1$ for all particle sizes. b) The imaginary permittivity converges to a value that does change with the nanoparticle size due to the size parameter x_m	22

3.2	Real 3.2a and imaginary 3.2b components of the permittivity according to the QCA approximation. As f tends to 1, the real component is able to reach the particle's permittivity while the imaginary component reaches zero which denotes a transition in the media.	23
3.3	Real and complex components corresponding to each model. The nature of the expansions can be seen more clearly by viewing the behaviour of both the a) Real and b) Imaginary permittivity. Although both theories offer good agreement in the results for $f < 0.05$, there is a large divergence in the behaviour in the imaginary component which may lead to drastically different results.	24
4.1	Experimental Kretschmann configuration with 4 layers. We have the BK7 prism as the first semi-infinite media; afterwards, the gold and the sample before reaching the semi-infinite air media. Light is picked up by the Photodetector which then sends the data to the computer to be analyzed later.	27
5.1	The experimental measurements (blue dots) plotted against the TMM model (blue line). The thickness of $38 \pm 0.12\text{nm}$ minimizes error function of the model with respect to the measurements and shows a good agreement with the experimental peak location.	28
5.2	a) Effective Medium's thickness over time. b) Adjustment of the TMM model of 4 layers to each measurement done.	29
5.3	a)	30
5.4	The fitted TMM model compared to the measurements of the samples immersed 30 seconds in BSA.	30

List of Tables

5.1	Estimated parameters of the Thiol-BSA Effective Medium using the TMM model by assuming a BK7-Gold-Sample-Air system. The estimated parameters of the sample are the real refractive index n_r , the imaginary refractive index n_i , the layer thickness d and the fitness score of the model R^2	29
5.2	Estimated average parameter models for both QCA and EFA for different BSA exposure times with a 95 % confidence interval. The volume filling fraction f and the surface coverage Ω_N are shown as percentages.	29
5.3	Tabulated estimated parameters for the BSA-CBZ effective medium using the TMM model assuming a BK7-Gold-Sample-Air medium.	30
5.4	Estimated effective medium parameters for the BSA-CBZ conjugate.	30

Contents

Abstract	v
List of Figures	vii
List of Tables	viii
1 Introduction	1
1.1 Motivation	1
1.2 Solution Overview	2
1.3 Thesis Organization	2
2 Surface Plasmon Polaritons	4
2.1 Electromagnetic Fields in Matter	4
2.2 Drude-Lorentz model	5
2.3 Surface Plasmons	7
2.3.1 TE mode	8
2.3.2 TM mode	9
2.4 Transfer Matrix Method	11
2.4.1 TMM Reflectance simulations for an IMI system.	13
2.4.2 TMM Reflectance simulations for a IMII system.	14
2.5 Gradient Descent	15
3 Effective Field Theory	17
3.1 Green's Function's applied to Helmholtz's equation	17
3.2 Approximation of Dispersion Relations	20
3.2.1 Considerations of the medium	20
3.2.2 Effective Field Approximation	21
3.2.3 Quasicrystalline Approximation	22
3.2.4 Simulation of EFA and QCA	24
4 Materials and Methods	26
4.0.1 Sample preparation	26
4.0.2 Experimental array	26
5 Results	28

6 Discussion	31
7 Conclusions and Future work	33
7.1 Conclusions	33
7.2 Future work	33
Bibliography	37

Chapter 1

Introduction

The field of plasmonics is a relatively new field of optics that was discovered in the early twentieth century when physicists were exploring the reflectance spectra arising from the interaction of light with metallic surfaces. In the experiments of Rayleigh and Wood [1, 2] it was found that by creating periodic structures on the surface of metals and illuminating the surface at a certain angle generated localized intensity anomalies at certain conditions which deviated from the traditional bulk behaviour. These anomalies are known as Rayleigh-Wood anomalies and their generation due to oscillating free-charges in the material are known as plasmons, which constitute the subject of study in the field of plasmonics. This specific type of anomaly was theoretically proposed in the early 50's yet it wasn't until the late 60's when Kretschmann proposed a theoretical and experimental description to generate it by using an Insulator-Metal-Insulator (IMI) structure [3]. This description, along with the introduction of the laser allowed for the Surface Plasmon Resonance (SPR) phenomena to be generated with enough consistency and precision for it to be used as a potential sensing tool.

In recent years the Kretschmann configuration has been used to sense a wide range of phenomena; from the detection of hazardous gases like NH_3 , CO or NO_2 [4, 5, 6, 7], to sensing bacteria and viruses for diagnostics [8, 9, 10, 11, 12], or detecting small concentrations of pollutants in air or liquid solutions [13, 14, 15]. All of these applications are possible due to the functionalization of a layer with a particular antibody for the selective detection of our material of interest; this by itself allows for the sensor to boast its label-free yet selective properties.

1.1 Motivation

Water is one of the substances in which we are more interested to detect pollutants since we rely on it not only for most of our industries, but also for the sustenance of human and animal life. SPR has been used before to sense trace pollutants like heavy metal particles [16] or pesticides like Atrazine [17] diluted in water since they can have a negative effect if consumed by either humans, animals or plants. One such substance of interest is Carbamazepine (CBZ): this is an active ingredient with anticonvulsant applications used in drugs for the treatment of

epilepsy. Recently however, concentrations of this drug have been found in water at a level that represents a threat [18]. Measurements of waste water have shown a concentration of 193ngL^{-1} while in the surface of clean water it was found at 17.2ngL^{-1} [19]. Although consumption of water with these trace concentrations of CBZ isn't harmful to humans; it has been found that these concentrations may be harmful or even fatal to microscopic algae and aquatic organisms [20]. Given that the aquatic ecosystem depends heavily on these microscopic organisms, it's of vital importance to monitor the CBZ levels in water.

There are many traditional methods that are used to detect trace concentrations pollutants in water like UV-Vis, Mass Spectroscopy and Chromatography. These methods yield valuable information about the composition of a solution and they can be used with conjunction with SPR to obtain a better characterization of a material, however the acquisition of the traditional tools requires additional spending which isn't always a possibility in an experiment. Therefore, it's of great interest to maximize the amount of information obtained from the tool we are using. In the case of SPR biosensors researchers tend to characterize the surface of the sensor with these previously mentioned methods, yet via the use of an alternative effective medium theory one can obtain a quantitative description of the functionalization only by using SPR measurements. Therefore, in this work a Surface Plasmon Resonance biosensor is built using the Kretschmann configuration. After this the gold surface is functionalized with Thiols and Bovine Serum Albumin (BSA) and a scattering model is used to determine the effectiveness of the functionalization using only SPR measurements. Finally, the measurements are done to detect the Carbamazepine adhesion to the functionalized surface via shifts in the resonance condition. All of these measurements are fitted to an analytical spectral model such that additional parameters of the measurements can be shown.

1.2 Solution Overview

The contributions of this thesis are.

- An automated SPR biosensor for the detection of Carbamazepine.
- A complimentary technique using this SPR sensor to characterize BSA deposition over time.
- A computational model to extract material parameters from intensity measurements.

1.3 Thesis Organization

In chapter 2 a derivation of the SPR phenomena from the wave equations are shown along with the Transfer Matrix Method formalism to simulate the propagation through homogeneous media; in chapter 3, Green's function's formalism is introduced along with the approximations of the dispersion media when considering spherical scattering. In chapter 4 the materials used to build the experimental array and the methods used to obtain the results are presented. Chapter 5 presents the results that are subsequently discussed in chapter 6. Finally, the conclusions

of this work are presented in chapter 7 along with potential routes of research one can follow after this project.

Chapter 2

Surface Plasmon Polaritons

Whenever an electromagnetic wave propagates through vacuum it will continue to do so undisturbed if it doesn't encounter any materials. However, in reality this is hardly the case since light ends up meeting matter sooner or later which brings up the field known as light-matter interactions. These may range from the traditional interactions like refraction to higher order scattering and coupling phenomena. This coupling phenomena tends to occur more frequently whenever noble metals are involved in optical frequencies which makes these materials the preferred choice to observe the SPR phenomena.

In this chapter, an analysis is done on Surface Plasmon Polaritons (SPP); first the dispersive behaviour of metals is modeled using the Drude-Lorentz model after which the behaviour of the surface plasmons is derived from the wave equation and boundary conditions; this derivation is done for an interface between 2 different media. After this, the Transfer Matrix Method is introduced as an alternative to calculate the Reflection and Transmission spectra of any incident light to an n-layer Kretschmann array. This is accompanied by simulations which show the behaviour of these reflection anomalies and a justification of why they can be used as biosensors.

2.1 Electromagnetic Fields in Matter

The behaviour of EM fields in matter can be described by the material parameters ϵ and μ which correspond to the electric permittivity and magnetic permeability of the material in question. The mathematical description of these fields is given by the macroscopic Maxwell's equations [21] which have the following form

$$\nabla \cdot \mathbf{D} = \rho_f, \quad \nabla \cdot \mathbf{B} = 0, \quad (2.1)$$

$$\nabla \times \mathbf{E} = -\frac{\partial \mathbf{B}}{\partial t}, \quad \nabla \times \mathbf{H} = \mathbf{J}_f + \frac{\partial \mathbf{D}}{\partial t}. \quad (2.2)$$

In these equations \mathbf{E} is the electric field and \mathbf{B} is the magnetic induction; however, there are two additional fields which are the electric displacement field \mathbf{D} and the magnetic field

H. These fields are derived from the primary fields in order to account for the interactions the \mathbf{E} and \mathbf{B} might have on the materials. To find these quantities one can introduce the general relations that relate both fields along with a material dependent quantity

$$\mathbf{D}(\mathbf{r}, t) = \epsilon_0 \mathbf{E}(\mathbf{r}, t) + \mathbf{P}(\mathbf{r}, t), \quad \mathbf{B}(\mathbf{r}, t) = \mu_0 (\mathbf{H}(\mathbf{r}, t) + \mathbf{M}(\mathbf{r}, t)), \quad (2.3)$$

where \mathbf{P} describes the polarizability of the material and \mathbf{M} describes the magnetization of the material. Since this thesis focuses on materials exposed to frequencies within the optical domain one can assume that $\mathbf{M} \approx 0$ given that the magnetization scales inversely with the frequency. In the general relation of the displacement field the polarizability can present a linear or non-linear dependence with respect to the electric field \mathbf{E} , if one works with materials in the linear regime then the relationship between \mathbf{P} and \mathbf{E} can be expressed as

$$\mathbf{P}(\mathbf{r}, t) = \epsilon_0 \chi(\mathbf{r}, t) \mathbf{E}(\mathbf{r}, t), \quad (2.4)$$

where the permeability χ contains all the information involving the effects of the field on the material; in the simplest case of a linear, isotropic, homogeneous and non-dispersive material then the displacement field can be directly related to the incident electric field via

$$\mathbf{D} = \epsilon_0 \epsilon \mathbf{E}, \quad (2.5)$$

where the material permittivity is defined as a constant $\frac{\epsilon}{\epsilon_0} = 1 + \chi$ and contains all the information of the response of the field; however, although the material permittivity is a constant for this ideal case, most materials will show some deviation from this behaviour. Therefore, a general model is a better approach when wanting to explore the behaviour of materials with more complex interactions; in order to describe the general behaviour of a linear material one needs to consider both spatial and temporal variations in the permittivity and the field. This results in the sum of the individual responses at each point in space which is defined as the convolution of the permittivity and the incident electric field

$$\mathbf{D}(\mathbf{r}, t) = \int dt' d\mathbf{r}' \epsilon(\mathbf{r} - \mathbf{r}', t - t') \mathbf{E}(\mathbf{r}, t). \quad (2.6)$$

By virtue of the convolution theory, this integral expression can be re-expressed as

$$\mathbf{D}(\mathbf{k}, \omega) = \epsilon_0 \epsilon(\mathbf{k}, \omega) \mathbf{E}(\mathbf{k}, \omega). \quad (2.7)$$

2.2 Drude-Lorentz model

Finding the analytical expression of the permittivity with respect to frequency is of great interest given that it allows for a way to predict the material's response when the incident temporal frequency changes. In the early 1900's Drude proposed a way one could approximate the permittivity of metals [22]; he did this by proposing a plasma model in which conduction electrons were modeled as dampened oscillators bound by an ionic core. Since we want to

approximate the behaviour of conducting materials when an electric field is applied we can add all of the forces using Newton's second law to obtain the following equation of motion

$$m \frac{d^2 \mathbf{x}}{dt^2} + m\gamma \frac{d\mathbf{x}}{dt} + m\omega_0^2 \mathbf{x} = -e\mathbf{E}, \quad (2.8)$$

where m is the electron mass, γ is a dampening constant relating to relaxation from an excited state and ω_0 is a potential resonance frequency of the electrons. This can correspond to both interband or intraband transitions inside the specific material and will result in a large absorption of the electric field. By assuming a harmonic time dependence of the electric field $\mathbf{E} = \mathbf{E}_0 e^{i\omega t}$ we know from the equation that our solution will be of the form ($\mathbf{x} = \mathbf{x}_0 e^{i\omega t}$). By plugging in this solution we're able to obtain an expression connecting $\mathbf{x}(t)$ and \mathbf{E}

$$\begin{aligned} \mathbf{x}_0 m(-\omega^2 + i\omega\gamma + \omega_0^2) &= -e\mathbf{E}_0, \\ \mathbf{x}_0 &= \frac{-e}{m(\omega_0^2 - \omega^2 + i\omega\gamma)} \mathbf{E}_0. \end{aligned}$$

The mean polarization of this array is given by the average charge displacement; assuming a constant number density n we can write the polarization as $\mathbf{P} = nex_0$.

$$\mathbf{P} = \frac{-ne^2}{m(\omega_0^2 - \omega^2 + i\omega\gamma)} \mathbf{E}_0.$$

This can then be substituted into the general expression of the displacement field.

$$\mathbf{D} = \epsilon_0 \mathbf{E} + \mathbf{P}, \quad (2.9)$$

$$\mathbf{D} = \epsilon_0 \left(1 - \frac{ne^2}{\epsilon_0 m(\omega_0^2 - \omega^2 + i\omega\gamma)} \right) \mathbf{E}_0. \quad (2.10)$$

By setting this equal to $\mathbf{D} = \epsilon_0 \epsilon \mathbf{E}$ we can extract the form of the dielectric function for a conductor

$$\epsilon(\omega) = 1 - \frac{\omega_p^2}{(\omega_0^2 - \omega^2 + i\omega\gamma)},$$

where ω_p is the plasma frequency of the material; this model is quite solid in explaining the dielectric properties of metals around a resonant frequency but fails when one gets far away from said frequency. This is due to the fact that this model only considers bound electrons and only considers a single resonant frequency while real atomic orbitals may have many; additional terms can be added to correct for those effects which will now turn the Lorentz model into the Drude-Lorentz model [23] which takes the form of

$$\epsilon(\omega) = \epsilon_\infty - \frac{\omega_p^2}{i\omega\gamma_D + \omega^2} - \sum_{n=1}^m \frac{A_n}{(\omega_n^2 - \omega^2 + i\omega\gamma_{L,n})}. \quad (2.11)$$

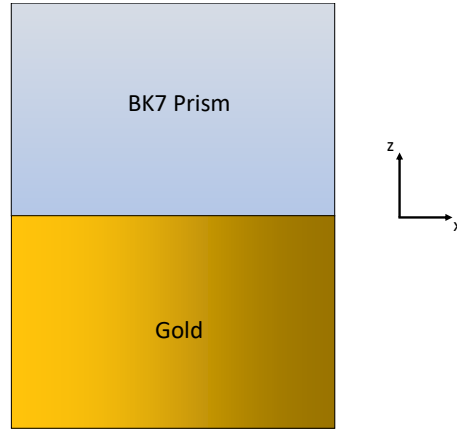


Figure 2.1: Schematic of a 2 layer system. The interface is located at $z = 0$ and both media are large enough to be considered infinite.

2.3 Surface Plasmons

Surface Plasmons originate due to the oscillation of a plasma in the surface/interface of a material; this oscillation ends up generating a new wave in response to the incident field. This is similar to how an evanescent wave is generated between two dielectrics and it even shares some properties like being confined in the direction normal to the interface and only propagating in the surface; however, these two are different in other aspects and this will have a stronger effect later on. In order to describe a general electromagnetic field we use the wave equation; however, assuming a harmonic time dependence $\frac{\partial}{\partial t} = i\omega$ lets us focus solely on the distribution of the field by using Helmholtz's equation

$$(\nabla^2 + k^2)\mathbf{E} = 0, \quad (2.12)$$

where ∇^2 is the Laplacian operator and k^2 is the magnitude of the wave vector $k = \sqrt{\epsilon}k_0$. Given that this comes from the wave equation, the same treatment can be done for the magnetic field \mathbf{H} . The relation between both fields can be found using Eq. 2.2 which gives

$$\mathbf{k} \times \mathbf{E}(z) = i\omega\mu_0\mathbf{H}(z).$$

Assuming we have an interface between 2 infinite media; we can select our coordinates in a way that make our problem easier to solve without loss of generality. Fig. 2.1 describes the configuration chosen where the $x - y$ plane is the boundary and z is the direction normal to the interface. By limiting the parallel component of the wave vector in the x direction then the field is homogeneous in y $\frac{\partial}{\partial y} = 0$ which allows us to write the electric field as

$$\mathbf{E} = \mathbf{E}(z)e^{i\beta x}. \quad (2.13)$$

In this function; the z and x dependence of the electric field is separable which will make differentiation easier; however, the $\mathbf{E}(z)$ term is a vector containing 3 unknown components

which means that the Helmholtz equation is a linearly separable system of differential equations. Given the previous considerations for the electric field the equation can be simplified to

$$\frac{\partial^2 \mathbf{E}(\mathbf{z})}{\partial z^2} + (k^2 - \beta^2) \mathbf{E}(\mathbf{z}) = 0. \quad (2.14)$$

This equation allows us to find the form of the z dependent electric field; given that the surface plasmons are confined in the direction normal to the interface we can assume that $\beta > k$ to obtain that $\mathbf{E}(z) = \mathbf{A}e^{-k_z z}$ where \mathbf{A} is a 3 dimensional vector. What follows is an analysis of our system utilizing the boundary conditions for both the \mathbf{E} and \mathbf{H} fields; however, instead of analyzing the 3 components of \mathbf{E} and \mathbf{H} at the same time decomposition of this general field can be made. In this case the most useful formalism is to divide the field into its transverse electric (TE) and transverse magnetic (TM) modes. In the TE mode only E_x and E_z are non zero while in TM only E_y is non zero, by using this we can analyze each mode independently to recover properties of the generated surface plasmon.

In a medium without any free charge or currents the boundary conditions are defined by the parallel and normal components of the fields in the following manner

$$\mathbf{E}_1^{\parallel} = \mathbf{E}_2^{\parallel}, \quad \epsilon_1 E_1^{\perp} = \epsilon_2 E_2^{\perp}, \quad (2.15)$$

$$\mathbf{H}_1^{\parallel} = \mathbf{H}_2^{\parallel}, \quad H_1^{\perp} = H_2^{\perp}. \quad (2.16)$$

Where the \perp and \parallel symbols corresponding to the field components parallel and perpendicular to the interface. Now that a set of coordinates is chosen and the boundary conditions are defined we can begin to solve this problem by solving each mode independently.

2.3.1 TE mode

In this mode the electric field only has a y component while the magnetic field has an x and z components; since the perpendicular component is the one in the z direction our boundary conditions can be written as

$$E_{y1} = E_{y2}, \quad (2.17)$$

$$\sqrt{\frac{\epsilon_1 \epsilon_0}{\mu_0}} \beta \cdot E_{y1} = \sqrt{\frac{\epsilon_2 \epsilon_0}{\mu_0}} \beta \cdot E_{y2}, \quad (2.18)$$

$$\sqrt{\frac{\epsilon_1 \epsilon_0}{\mu_0}} k_{z1} \cdot E_{y1} = \sqrt{\frac{\epsilon_2 \epsilon_0}{\mu_0}} k_{z2} \cdot E_{y2}. \quad (2.19)$$

Where the fields are evaluated at $z = 0$ and an undefined x , by plugging in our expressions for the field from Eq. 2.13; we reach the following condition regarding the dispersion relation of the perpendicular wave vector component k_z

$$A_y e^{i\beta x} \frac{\epsilon_0}{\mu_0} (k_{z1} + k_{z2}) = 0. \quad (2.20)$$

From this expression we note that the sum of each perpendicular wave vector isn't 0 since both are positive quantities. $\epsilon_0/\mu_0 \neq 0$ and the exponential isn't always zero. This means that the only way for this condition to be valid is for the amplitude of the electric field to be equal to zero which means that there won't be a surface plasmon generated for TE polarized waves. From here we can now focus on the remaining polarization to test for an additional condition.

2.3.2 TM mode

In this mode the electric field now has 2 components (x, z) while the magnetic field only has the y component. By following a similar procedure as before [24] we can evaluate our boundary conditions as follows

$$E_{x1} = E_{x2}, \quad (2.21)$$

$$\epsilon_1 E_{z1} = \epsilon_2 E_{z2}, \quad (2.22)$$

$$(\beta E_{z1} - k_{z1} E_{x1}) = (\beta E_{z2} - k_{z2} E_{x2}). \quad (2.23)$$

By combining Eq. 2.18 and 2.19 one can recover the following expressions relating the field magnitudes without any oscillating components

$$|E_{1x}| = |E_{2x}|, \quad (2.24)$$

$$\epsilon_1 E_{1z} = \epsilon_2 E_{2z}. \quad (2.25)$$

By plugging these into the third condition, we can recover a non-trivial dispersion relation for k_z and k_x , namely

$$\beta E_{z1} \left(\frac{\epsilon_2 - \epsilon_1}{\epsilon_2} \right) = E_x (k_{z1} - k_{z2}). \quad (2.26)$$

We can define the field components in terms of the parallel and perpendicular field components by using $\nabla \cdot \mathbf{D} = 0$ at each medium, which results in the following expression relating both fields $\beta E_x + k_z E_z = 0$. By substituting the z field in terms of E_x we get the dispersion relation for the propagation of the surface wave along the interface

$$\beta^2 = (k_{z1} - k_{z2}) k_{z1} \left(\frac{\epsilon_2}{\epsilon_2 - \epsilon_1} \right), \quad (2.27)$$

$$\beta = k_0 \sqrt{\frac{\epsilon_1 \epsilon_2}{\epsilon_1 + \epsilon_2}}. \quad (2.28)$$

When one is looking for any type of resonance phenomena, it's recommended to find discontinuities in the dispersion relation. For this case the resonance condition is given as $\epsilon_1 = -\epsilon_2$, since that would lead to the divergence of the plasmon propagation constant β . For this to happen the real components of their respective dielectric functions need to have opposite signs which is usually the case with metals and dielectrics in the optical regime.

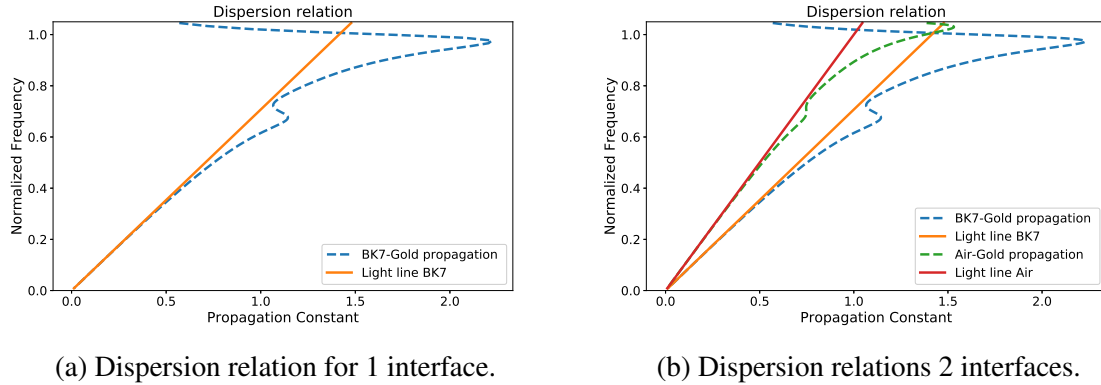


Figure 2.2: Dispersion relations including the plasmon propagation constant. a) For the two layer system the light line and the propagation constant can be identified yet they only cross at the bulk plasmon resonance ($y = 1$). b) For the 3-layer system the light lines may cross at points other than the bulk plasmon resonance, this intersection allows for the coupling of light and generation of the Surface Plasmon Resonance.

The dispersion relations for β and k_1 are shown in Fig 2.2a. The simulation was done by using the Drude-Lorentz model in Eq. 2.11 and adjusted using the parameter values in [25]. We will notice that the intersection of the curve takes place at a frequency where $\epsilon_1 = -\epsilon_2$, which corresponds to the bulk plasma frequency of gold. However, we are interested in a surface plasmon which occurs whenever an medium's dispersion curve intersects the beta curve before the plasma frequency. In order to achieve this condition one would have to introduce an additional material into the system which will cause additional resonance. When that occurs the surface modes of the plasmons couple with the incident light and a surface mode occurs; this system can be visualized in Fig. 2.3.

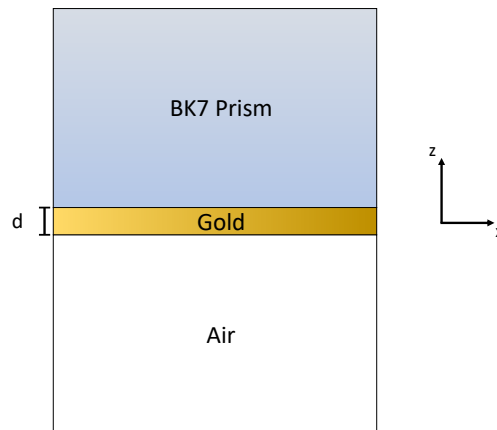


Figure 2.3: A 3 layer system (also known as the Kretschmann configuration) made of a BK7 prism, a gold layer of thickness d and an infinite outer medium of air. Given this system and the dispersion relation in 2.2b any light incident from the BK7 prism will generate a plasmon mode in the Air-Gold interface.

So when one has a system with at least three layers then the SPR phenomena can be

obtained via coupling; however, this isn't limited exclusively to 3-layer systems. One can engineer multilayer systems or even large periodic structures which can extend from 3 to even 10 or more layers. One could potentially test the configurations using the same method as before yet the analytical expressions of the plasmon propagation become tedious to solve. Therefore, a different method is used in order to simulate the propagation of the incident electric field along any multilayered system via the use of 2x2 matrices.

2.4 Transfer Matrix Method

The Transfer Matrix Method (TMM) [26] exists as a way to facilitate the simulation of multilayered systems, this method has seen a large use in SPR biosensor design via simulations since it allows for the calculation of reflectance and transmittance, which are used to determine the resonance conditions and the sensitivity of our sensor. Another reason why this is so compatible with this particular application is that the input parameters of this model are the layer's thickness and permittivity which are key factors in achieving resonance condition. An additional use of this is that it allows for the simulation of a sensor with any number of layers like in Fig. 2.4.

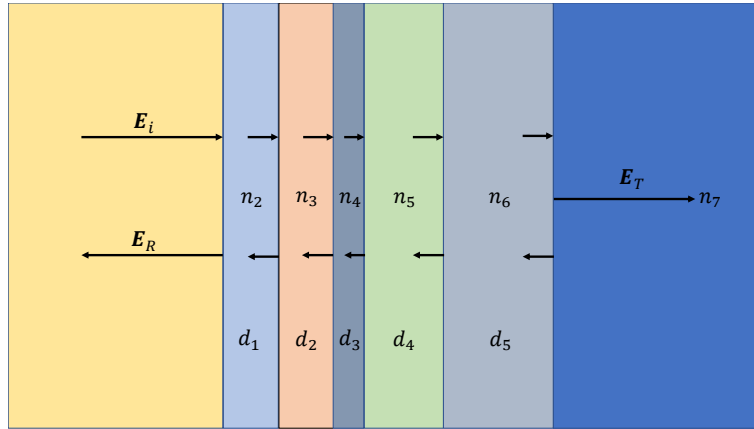


Figure 2.4: Visualization of a system where the TMM can be applied; the fields on the left side correspond to the incident E_i and reflected E_r fields while the field on the right hand side is the transmitted field E_t . Each of the finite layers is characterized by a thickness d_i and refractive index n_i .

This method works by representing the effect of each interface and layer with a matrix; doing so allows to operate these matrices onto a field of interest which will result in a method similar to the ray transfer matrix except that this method is applied to electric fields. One can represent this propagation using the following formula

$$\begin{bmatrix} E_i \\ E_r \end{bmatrix} = \mathbf{M} \begin{bmatrix} E_t \\ 0 \end{bmatrix}, \quad (2.29)$$

where E_i is the incident field, E_r is the reflected field and E_t is the transmitted field, while \mathbf{M} is a 2x2 matrix with unknown coefficients. In order to explore the behaviour of the method we

can inspect the case of system with 2 layers (the one we analyzed for the bulk plasmon in the previous section). This corresponds to having only one interface which results in the simplest possible case to simulate with this method. Before trying to find the coefficients of the matrix we define Fresnel's coefficients [27] which tell us the relationships between the amplitudes of the incident, transmitted and reflected fields, given by

$$E_r = rE_i, \quad E_t = tE_i. \quad (2.30)$$

where r indicates the reflection coefficient and t is the transmission coefficient. By using these relations and multiplying the matrix by the right hand vector we get a system of 2 equations and 2 unknowns. The elements of the matrix are the coefficients relating the response of the boundary with respect to the incident field.

$$E_i = M_{11}E_t, \quad \frac{E_t}{E_i} = \frac{1}{M_{11}} = t, \quad (2.31)$$

$$E_r = M_{21}E_t, \quad \frac{E_r}{E_i} = \frac{M_{21}}{M_{11}} = r. \quad (2.32)$$

From these equations we can write the matrix elements (1,1) and (2,1) in terms of the reflection and transmission coefficients.

$$M_{11} = \frac{1}{t}, \quad M_{21} = M_{11}r = \frac{r}{t}. \quad (2.33)$$

In order to find out the form of the second column one would need to study the behaviour of a slightly more complex system of 3 layers, which won't be done in this thesis and can be consulted in the following resource [28]. This ends up giving the boundary matrix the following form

$$\mathbf{M} = \frac{1}{t} \begin{bmatrix} 1 & r \\ r & 1 \end{bmatrix}. \quad (2.34)$$

This matrix offers a valid description for the boundary between two semi-infinite media. However, when studying the $n + 1$ layer system the phase change induced by the propagation of the field through different media needs to be taken into account. Doing so, the matrix representing additional boundaries takes the following form, where waves travelling in 2 different directions are taken into account

$$\mathbf{M}_i = \frac{1}{t_i} \begin{bmatrix} e^{-ik_{i,\perp}d_i} & 0 \\ 0 & e^{ik_{i,\perp}d_i} \end{bmatrix} \begin{bmatrix} 1 & r \\ r & 1 \end{bmatrix}, \quad (2.35)$$

where $k_{i,\perp}d_i = n_i k_0 d_i \cos(\theta_i)$ and the i 'th index corresponds to the i 'th finite layer of thickness d_i . Now with this new propagator matrix we can calculate the final state for any system of $n + 1$ layers via the following formula.

$$\mathbf{M}_{\text{sys}} = \prod_{i=1}^n \mathbf{M}_i. \quad (2.36)$$

After calculating the system matrix one can calculate the system's reflection coefficient the same way it was defined in Eq. 2.13, except that the coefficients correspond to the final matrix. With this result we can now simulate any 1D system we want and engineer the input and layer parameters to obtain a desired response based on the application desired application or line of research. What follows are examples of some simulations done for our specific application of an SPR biosensor using a 3 and a 4 layer system.

2.4.1 TMM Reflectance simulations for an IMI system.

By limiting the system to only 3 components, one can explore a smaller subset of parameters and results from which we can visualize the effectiveness of this configuration as a way to sense sample. The input parameters of this 3 layer system are.

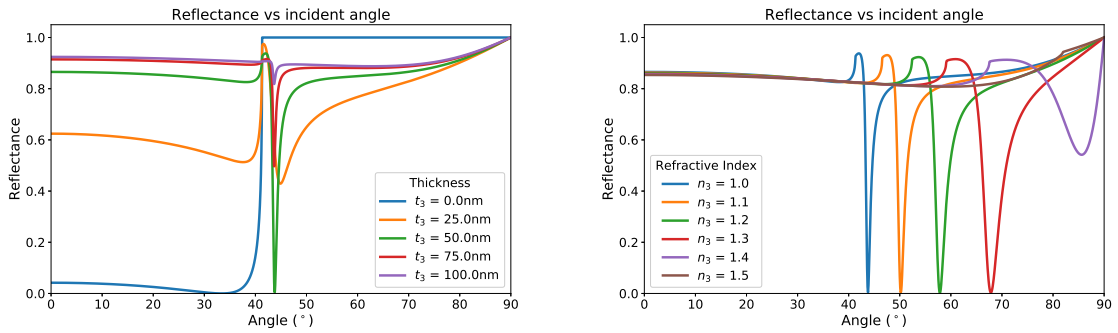
- An incident light beam with a fixed wavelength λ and travelling at an incident angle θ_i
- An initial dielectric with a purely real permittivity $\sqrt{\epsilon_1} = n_1$ and an infinite thickness.
- A metallic nanolayer of a complex refractive index $n_2(\omega)$
- A metallic layer of thickness d .
- An output dielectric layer with a purely real permittivity n_3 and an infinite thickness.

Yet out of these parameters there are a few that can fixed in the simulations due to the available experimental materials like the wavelength $\lambda = 633\text{nm}$ corresponding to a HeNe laser, the initial dielectric $n_1 = 1.514$ (BK7 prism) and the metallic nanolayer made of gold $n_2 = 0.178 - 3.44i$ are fixed. The selection of these features were based on the standard configuration choices of SPR biosensors (Gold and BK7 prism) [29]. With these fixed parameters in mind; the two remaining parameters were modified in order to visualize the variations in the signal response. In Fig 2.5a, the effects of changing the metal's thickness while keeping the other parameters constant can be observed. In Fig 2.5b, the additional effect of changing the refractive index of the output media is analyzed as well. These images allow us to get an idea of the range of values our 2 free parameters may take that given the physical phenomenon we're studying.

From these simulations one can determine that the gold nanolayer thickness is bounded between 0-100nm and the output refractive index is bounded between 1-1.514 RIU. When translating this to an experimental situation of performing measurements using the same prism and gold layer but with different samples we obtain similar observations to those seen in Fig. 2.5b. That is; if the properties of the sample change then this will translate to a different refractive index and to a different resonance angle. It is the process of associating this refractive index change with a physical or chemical change in the sample that allows for the sensing

applications of this phenomena.

An important consideration to keep in mind is the sensitivity of the resonance angle to changes in the exiting media's refractive index. At small values of n_3 the sensitivity can be as high as $60^\circ(\text{RIU})^{-1}$; that is, the resonance angle is translated 60 degrees when the exiting media has a refractive index of 2. This would seem good yet issues arise when considering that the sensor's sensitivity isn't constant, it actually starts to decrease as the resonance angle increases so the effective range of our sensor is in fact 1.0-1.2 RIU. By limiting the angular resolution to 0.1° which corresponds to traditional angular resolutions then for this configuration the sensitivity is $0.0016 \frac{\text{RIU}}{\text{deg}}$.



(a) Structure with $n_3 = 1$ and varying d .

(b) Structure with $d = 50\text{nm}$ and varying n_3

Figure 2.5: Simulations of IMI structures taking into account variations of the gold and last insulator. a) The gold's thickness is varied. At thicknesses below 25nm the phenomena approaches the behavior of total internal reflection while at thicknesses above 75 the plasmonic response is minimized as the bulk behaviour is achieved. b) The output refractive index is varied. Changes in the refractive index cause a shift in the SPR angle yet as the refractive index approaches that of BK7 the plasmonic response disappears.

2.4.2 TMM Reflectance simulations for a IMI system.

Although 3 layers are usually enough for some SPR applications, sometimes additional surfaces are added to the system due to functionalization (adding antibodies to allow for attachment of a sample) or to the tuning of the physical parameters of the sensor (sensitivity and dynamic range). In principle this is geometrically similar to the 3 layer case except that there is one additional finite layer of thickness δ_3 . Just like in the previous case the input parameters for the TMM simulation are shown.

- Incident media is BK7 $n_1 = 1.514$
- Electric field with $\lambda = 633\text{nm}$ travelling to the first interphase with an angle θ_i .
- Second layer made of gold $n_2 = 0.178 - 3.44i$ and $\delta_2 = 50\text{nm}$.
- Output media is air $n_4 = 1$

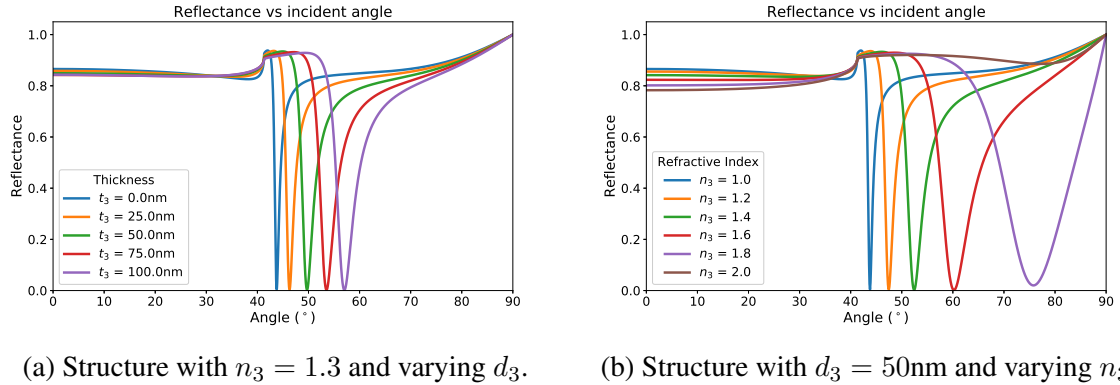


Figure 2.6: Simulations of IMII structures taking into account variations of the third layer's properties. a) Variations of the layer's thickness with a fixed refractive index shows that despite a large thickness of 100nm the plasmonic response isn't diminished. b) Variations of the refractive index with a fixed thickness show that the IMII system has a wider dynamic range while being able to detect a refractive index of 1.8 RIU.

The only free parameters of the system correspond to the third layer from which we can vary the thickness d_3 and the refractive index n_3 . The effects of changing the refractive index of the third layer can be seen in Fig. 2.6b for a thickness of 50nm while the effects of the thickness can be visualized in Fig. 2.6a where the refractive index is fixed at 1.3 which was out of the range of the previous sensor.

From this simulations it can be seen that the properties of the sensor have greatly improved when compared to the 3 layer sensor. There is a wider refractive index dynamic range (1-1.8) and layers of up to 75nm can be detected; however, there is a disadvantage with this increased range. In experimental measurements one has a limited angular resolution to obtain the reflectance measurements; if the angular resolution is too high then the sensor might not be able to distinguish between 2 different refractive indexes. Therefore, that needs to be taken into consideration whenever one builds an SPR sensor.

2.5 Gradient Descent

In order to adjust the SPR reflectance measurements with the theoretical curves one can use an optimization method to do so; in this case the gradient descent method will be used due to the availability of an analytical expression and the ease of programming the method. The way this method works is similar to Newton's method in principle; however, instead of using a matrix operator this one combines the use of a gradient operator and a concave error function [30]. The most commonly used function in this type of problems is the mean squared error function since it's normalized for any arbitrary amount of points, it has a minimum value of 0 and it's guaranteed to have at least one minima due to the function being raised to the second power

$$\text{MSE} = \frac{1}{2N} \sum_{i=1}^N (y_i - \hat{y}_i)^2, \quad (2.37)$$

where N corresponds to the number of data points we have available, y_i are the measured values and \hat{y}_i is the model's estimation for that point. In the case where the model depends solely on one variable the minima is found by calculating the derivative and setting it equal to 0; however, in the case of the a multivariate function the gradient operator is used which involves calculating the partial derivative over every variable. If one applies the gradient operator to the mean squared function the resulting vector is

$$\nabla \text{MSE} = \frac{1}{N} \sum_{i=1}^N (y_i - \hat{y}_i) (-\nabla \hat{y}_i), \quad (2.38)$$

where the gradient will result in a $1 \times n$ vector where n corresponds to the number of variables being optimized. This vector will be pointing to the direction where the function will experience the maximum growth; therefore, in order to obtain the direction of greatest decrease in value all that's needed is to add a negative sign. This leaves the following iterative formula for gradient descent

$$\mathbf{x}_{i+1} = \mathbf{x}_i - \gamma \nabla F(\mathbf{x}_i), \quad (2.39)$$

$$\mathbf{x}_{i+1} = \mathbf{x}_i + \frac{\gamma}{N} \sum_{i=1}^N (y_i - \hat{y}_i(\mathbf{x}_i)) (\nabla \hat{y}_i(\mathbf{x}_i)), \quad (2.40)$$

where \mathbf{x} is the vector containing the n variables to be estimated and γ is a carefully selected constant in order to regulate the speed of convergence. The selection of this constant is important since if the constant is too large the method will miss the global solutions and it might even diverge, however, if the value is too small then the speed of convergence will be small as well and one might become trapped in a local minimum without reaching the global solution.

Chapter 3

Effective Field Theory

In the previous section we have shown how we're able to extract information from a small layer of material using the SPR phenomena and the TMM method; however, we are assuming that the layers are perfectly homogeneous which is a valid assumption if the deposition process was done carefully or if the thickness is larger than the dimensions of the constituents. If the dimensions of the constituents is comparable to the layer thickness then the situation becomes more complicated since the homogeneous layer assumption is no longer valid. This can end up affecting performance of the sensor since the functionalization might not be as effective which will result in a decrease of the sensor's response. A traditional approach to characterize the quality of functionalization, would be to use other characterization techniques to test for surface deposition like spectroscopy or even electron microscopy which are completely valid approaches; however, this isn't always possible in research since the machines needed to perform these techniques are often very expensive. Therefore, a theory that is able to describe this complex medium's constituents and relate them to an equivalent homogeneous layer would allow for the quantitative characterization of the functionalization.

In this chapter, we'll begin by introducing the concept of Green's function and how it can be used to solve the Helmholtz equation containing source terms. Afterwards, the problem of multiple spherical scatterers will be where certain considerations will be shown in order to arrive at 2 distinct approximate dispersion relations. These will then be introduced and simulated for the calculation of 2 new parameters of interest which are the volume filling fraction and the mean particle radius.

3.1 Green's Function's applied to Helmholtz's equation

Helmholtz's equation is defined as a linear differential equation, this means that the equation can be represented in the form of

$$\mathbf{L}E = f, \tag{3.1}$$

where \mathbf{L} is an operator, E is the solution and f corresponds to one or multiple source terms which end up interacting with the field. What's usually done in these cases is that one considers a specific geometry to solve like in the previous section and then the equation is solved

either analytically or by proposal of an Ansatz to extract a dispersion relation. The issue here is that whenever there is a change in the domain or the boundary conditions the process would need to be repeated for new operators or source terms. A solution to this situation can be found by proposing the simplest possible source term for the equation: the Dirac Delta function which turns the previous equation into

$$\mathbf{L}E = \delta(s - x). \quad (3.2)$$

In the case of a linear differential operator, this problem has a unique solution which will change in response to any changes in the domain. The function that solves this problem is known as Green's function [31] which is any function that satisfies the following equation

$$\mathbf{L}G(x, s) = \delta(s - x), \quad (3.3)$$

where s is a parameter that will describe the translation dependency of the linear operator \mathbf{L} . If there is no such dependency then Green's function can be written in terms of $G(x - s)$ and the solution can be written in terms of the superposition of Green's functions in a region of space. The main use of this function is to find its analytical form and then use it to find the solution for any source term via a convolution operation, it is in this convolution where the boundary conditions are taken into account. In the case of the scalar inhomogeneous Helmholtz's equation with a point source in an arbitrary media described by the wave vector amplitude $k = \omega^2 \mu \epsilon$, the differential equation that yields Green's function for this operator is

$$(\nabla^2 + k^2)g = -\delta(r - r'), \quad (3.4)$$

where g represents Green's function, $\nabla^2 + k^2$ represents the linear operator of the equation and $\delta(r - r')$ is the Dirac delta function which is used to represent the point source. In order to find an analytical solution, the Fourier transform is applied to this equation which leads to the following form of Green's function

$$g(r, r') = g(r - r') = \frac{e^{ik|r-r'|}}{4\pi|r-r'|}, \quad (3.5)$$

this form of the function is the form of a spherical wave with unit amplitude. If one wants to extend the analysis of this function for the 3 dimensional Helmholtz equation, then the equation needs to be written in operator form as

$$\nabla \times \nabla \times \overline{\overline{G}} - k^2 \overline{\overline{G}} = \overline{\overline{I}} \delta(r - r'), \quad (3.6)$$

where $\overline{\overline{I}}$ corresponds to the unit dyadic operator and $\overline{\overline{G}}$ is the dyadic Green function. The dyadic form of the Green function can be recovered from the original solution we found before via the following operator

$$\overline{\overline{G}} = \left(\overline{\overline{I}} + \frac{1}{k} \nabla \nabla \right) g(r, r'). \quad (3.7)$$

With that in mind then Eq. 3.6 now fully represents the Helmholtz equation in a homogeneous media containing one source; however, we're interested in exploring the behaviour of this equation when the domain isn't homogeneous. For this we can assume a simple case of a spherical particle with radius a and an associated wavevector k . This would lead to a modification to the differential equation in terms of a space dependent permittivity and to two distinct Green's functions: one for free space and one for the particle. This new piece-wise equation takes the following form

$$\nabla \times \nabla \times \overline{\overline{G}}_s - k_m^2 \overline{\overline{G}}_s = \overline{\overline{I}} \delta(\mathbf{r} - \mathbf{r}') + (k^2(r) - k_m^2) \overline{\overline{G}}_s, \quad (3.8)$$

where $\overline{\overline{G}}_s$ is Green's function and k is a piece-wise function depending on our position in space. If we're inside the particle then it's equal to the k_p of the particle while outside of the particle it's equal to that of the medium k_m . This will make it so the equation applies for every region in space which allows us to write Green's function of this new equation as a weighted sum of the functions in different regions of space

$$\overline{\overline{G}}_s(r, r') = \overline{\overline{G}}_0(r, r') + \int_{V_p} d\mathbf{r} \overline{\overline{G}}_0(r, r'') (k_p^2 - k_m^2) \overline{\overline{G}}_s(r'', r'), \quad (3.9)$$

where V_p corresponds to the region of space where the particle of interest is located. This integral will give as a result Green's function for the case of a single spherical particle in a medium. In order to ease the transition to a multiple particle problem it's useful to replace the integrals and functions by their equivalent operators; although the function is still the same, this helps the visualization and treatment of the functions. The scattering operator takes the form of

$$\overline{\overline{G}}_s = \overline{\overline{G}}_0 + \overline{\overline{G}}_0 \overline{\overline{U}} \overline{\overline{G}}_s, \quad (3.10)$$

where $U = (k^2 - k_m^2)$ is analogous to a potential function. In order to expand it to N particles we would just need to add all the volume integrals in every sphere of all space, for the next equation the s subscript will be dropped since it can't refer to a single scatterer now

$$\overline{\overline{G}} = \overline{\overline{G}}_0 + \sum_{l=1}^N \overline{\overline{G}}_0 \overline{\overline{U}}_l \overline{\overline{G}}. \quad (3.11)$$

To obtain a full description of this scattering medium one should take into account the configurational average of the particles. Specifically, the dependence this average might have with respect to other quantities since in [32] it is shown that this average depends on the average assuming one particle is fixed. This one depends on the average with 2 particles fixed and it continues going in this pattern. This leads to a very large system of hierarchical equations which need to be truncated at a certain point in order to reach an analytical solution. The

dispersion relations reached at the first order and second order truncations will be analyzed during the remainder of the chapter under the low frequency assumption. If one is interested in the complete derivation of these equations they may consult the following resource [33].

3.2 Approximation of Dispersion Relations

3.2.1 Considerations of the medium

In the approximations of the dispersion relations there are 2 additional material parameters that are considered in the calculations: The volume filling fraction f and the particle radius a . Out of these two the first one can be used to derive an additional property of the material which is the surface coverage Ω , these two quantities are defined as

$$f = \frac{N \frac{4}{3} \pi a^3}{V_0}, \quad (3.12)$$

$$\Omega = \frac{N \pi a^2}{A_0}, \quad (3.13)$$

where Ω is the percentage of the surface area covered by the particles, N is the number of particles, A_0 is the total area of the surface the particles are in contact with and V_0 is the total volume of the medium being studied. Therefore, Ω and f represent the total area and volume occupied by the particles. In the case of a monolayer one can assume that the total volume takes the form of $V_0 = A_0 2a$; by plugging this into the previous expression of f and setting $f = C\Omega$ one can reach the following relation.

$$f = C\Omega, \quad (3.14)$$

$$\frac{N \frac{4}{3} \pi a^3}{A_0 2a} = C \frac{N \pi a^2}{A_0}, \quad (3.15)$$

$$\frac{2}{3} = C. \quad (3.16)$$

Under these assumptions the surface coverage can be calculated by the use of the volume fraction $\Omega = \frac{3}{2}f$. Since the surface coverage is a fraction, the value of Ω is bounded between zero and one. This places a constraint on the maximum volume filling fraction at $\frac{2}{3}$ since any greater value will result on a surface coverage exceeding one. This constant can change depending on how many layers one considers in their analysis but for any case considering spheres filling up rectangular volumes, the volume fraction will never reach one.

Another important detail to consider is that in the case of a monolayer the surface will never be fully covered when considering spherical particles. This can be seen by considering the configuration at which spheres have the highest packing density, by doing the maximum surface area covered by a monolayer at this configuration it's found that the maximum coverage is $\frac{\pi}{4} \approx 0.785$. Therefore, the maximum surface coverage possible in a monolayer

configuration is 0.785 which further reduces the maximum filling fraction to 0.471. With this in mind a normalized surface coverage can be defined as

$$\Omega_N = \frac{1.5f}{0.785}, \quad (3.17)$$

where Ω_N is the normalized surface coverage and can range from zero to one where one represents the maximum surface coverage possible by spheres forming a monolayer.

3.2.2 Effective Field Approximation

If one stops the calculation after fixing only one particle, this will result in a case where the particles aren't interacting with each other. This will result in measurement of the phenomenon that highly impact the resulting media but only at sparse concentrations, this reduction of effects is why this is known as the Effective Field Approximation. Combined with the previously mentioned low frequency approximation this results in the following dispersion relation for the effective medium

$$\epsilon = \epsilon_m + 3\epsilon_m f \gamma \left(1 + i \frac{2x_m^3 \gamma}{3} \right), \quad (3.18)$$

$$\gamma = \frac{\left(\frac{\epsilon_p}{\epsilon_m} - 1 \right)}{\left(\frac{\epsilon_p}{\epsilon_m} + 2 \right)}, \quad (3.19)$$

where ϵ is the effective permittivity of the medium, ϵ_m is the permittivity of the medium the particles are suspended in, f is the volume fraction the particles occupy, γ is equal to the Clausius-Mossotti factor of the medium and $x_m = k_m a$ is the size parameter where a is the radius of the scattering particle. In this case we note that the approximation is linear in terms of the volume fraction and that it considers both a real and imaginary component of the refractive index where that imaginary component is related to the scattering effects of the spheres. It is also noted that the real and imaginary components of the permittivity are separable which yields the following equations

$$\epsilon_r = \epsilon_m (1 + 3f\gamma), \quad (3.20)$$

$$\epsilon_i = 2\epsilon_m^{\frac{5}{2}} k_0^3 a^3 \gamma^2 f. \quad (3.21)$$

These two permittivity components can be simulated independently for different values of f and a which can be observed in Fig. 3.1a and Fig. 3.1b. For these simulations the parameters of $\epsilon_p = 3.57$, $\epsilon_m = 1$ and $\lambda = 633\text{nm}$; it's important to note that although the previous section established a maximum volume filling fraction of 0.471 due to the consideration of a particle monolayer, the simulations will filling fractions from 0 to 1 which can occur yet the medium at that point may no longer be considered a particle monolayer.

For the application of an SPR biosensor one usually works from the refractive index measurements and recovers the volume fraction and particle radius rather than the other way around. Given that we have two equations with two unknown parameters (f and a) we are able to obtain an analytical expression for the volume fraction and the radius

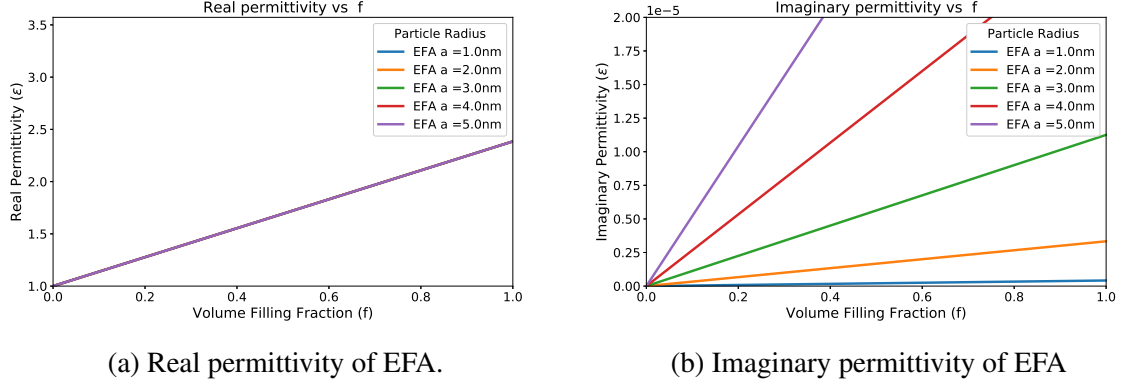


Figure 3.1: Simulation of permittivity components according to EFA, both components showing a linear behaviour with respect to f . As f approaches one: a) The real permittivity converges to $3\gamma + 1$ for all particle sizes. b) The imaginary permittivity converges to a value that does change with the nanoparticle size due to the size parameter x_m .

$$f = \frac{\left(\frac{\epsilon_r}{\epsilon_m} - 1\right)}{3\gamma}, \quad (3.22)$$

$$a = \left(\frac{\epsilon_i}{2\epsilon_m^{\frac{5}{2}}k_0^3\gamma^2 f}\right)^{\frac{1}{3}}. \quad (3.23)$$

3.2.3 Quasicrystalline Approximation

If one considers the 2nd term of the hierarchy of equations and again use the low frequency approximation then they reach the following dispersion relation

$$\epsilon = \epsilon_m + \frac{3\epsilon_m f \gamma}{1 - f \gamma} \left(1 + i \frac{2x_m^3 f \gamma^2 (1 - f)^4}{(1 - f \gamma)^2 (1 + 2f)^2}\right). \quad (3.24)$$

Although no new variables have been added to the model, it has a more complex form by involving non-linear dependencies of f which leads to a behaviour that adheres closely to the . Despite the additional complexity one has by considering additional interactions between particles, this dispersion relation can be separated into its real and complex components as well which allows for the analytic calculation of the volume filling fraction and the particle radius

$$\epsilon_r = \epsilon_m \left(1 + \frac{3f\gamma}{1 - f\gamma} \right), \quad (3.25)$$

$$\epsilon_i = \frac{2\epsilon_m^{\frac{5}{2}} k_0^3 a^3 f \gamma^2 (1 - f)^4}{(1 - f\gamma)^2 (1 + 2f)^2}. \quad (3.26)$$

This in turn allows for a similar procedure to the one done in the previous section to take place in which the real and imaginary components of the permittivity can be simulated by varying the volume filling fraction and the nanoparticle size. The results of these simulations can be seen in Fig. 3.2 with the same parameters as before. Instantly the difference in behaviour can be seen since now the real permittivity does reach the particle permittivity for a volume fraction of one while the imaginary component is bounded and approaches zero in the same case.

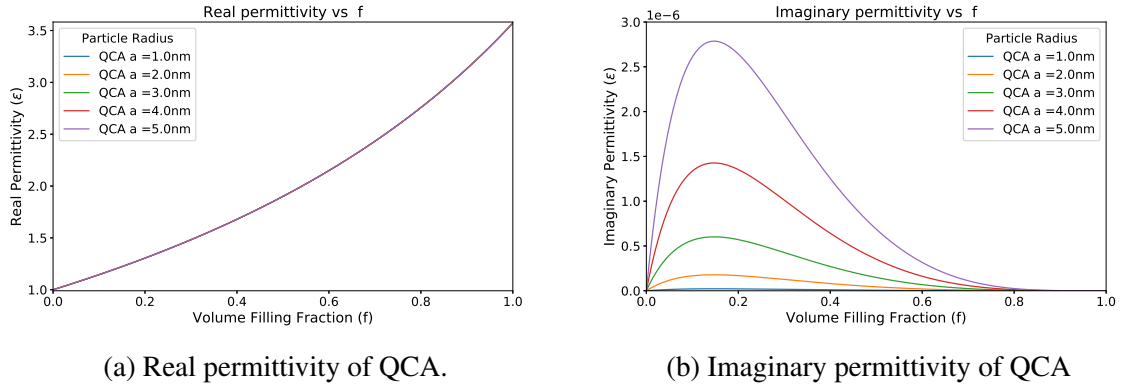


Figure 3.2: Real 3.2a and imaginary 3.2b components of the permittivity according to the QCA approximation. As f tends to 1, the real component is able to reach the particle's permittivity while the imaginary component reaches zero which denotes a transition in the media.

Although the relationship of the permittivity's components with respect to f and a have become more complex, it's still possible to recover 2 equations that give values of f and a for given values of measured permittivities. Starting with the real part one can recover the volume fraction

$$\frac{\epsilon_r}{\epsilon_m} = 1 + \frac{3f\gamma}{1 - f\gamma}, \quad (3.27)$$

$$f\gamma \left(\frac{\epsilon_r}{\epsilon_m} + 2 \right) = \frac{\epsilon_r}{\epsilon_m} - 1, \quad (3.28)$$

$$f = \frac{\left(\frac{\epsilon_r}{\epsilon_m} - 1 \right)}{\gamma \left(\frac{\epsilon_r}{\epsilon_m} + 2 \right)}. \quad (3.29)$$

This result can be seen as a ratio of the Clausius-Mossotti factor and it's equal to one whenever the medium's factor is equivalent to that of the particle. Using the imaginary component one can recover a formula for the radius in terms of f

$$a^3 = \frac{\epsilon_i(1 - f\gamma)^2(1 + 2f)^2}{2\epsilon_m^{\frac{5}{2}}f\gamma^2(1 - f)^4}, \quad (3.30)$$

$$a = \left(\frac{\epsilon_i(1 - f\gamma)^2(1 + 2f)^2}{2\epsilon_m^{\frac{5}{2}}k_0^3f\gamma^2(1 - f)^4} \right)^{\frac{1}{3}}. \quad (3.31)$$

With these two functions, one can work with SPR measurements in order to extract material properties.

3.2.4 Simulation of EFA and QCA

The following section will show a comparison between the first and second order approximation. Both models will have the same parameters used in the previous section $\epsilon_m = 1$, $\epsilon_p = 3.57$, $\lambda = 633\text{nm}$ but now the nanoparticle radius will be fixed at $a = 30\text{nm}$. The results are shown in Fig. 3.3a and Fig. 3.3b and show the distinct behaviour of both the first and second order approximations.

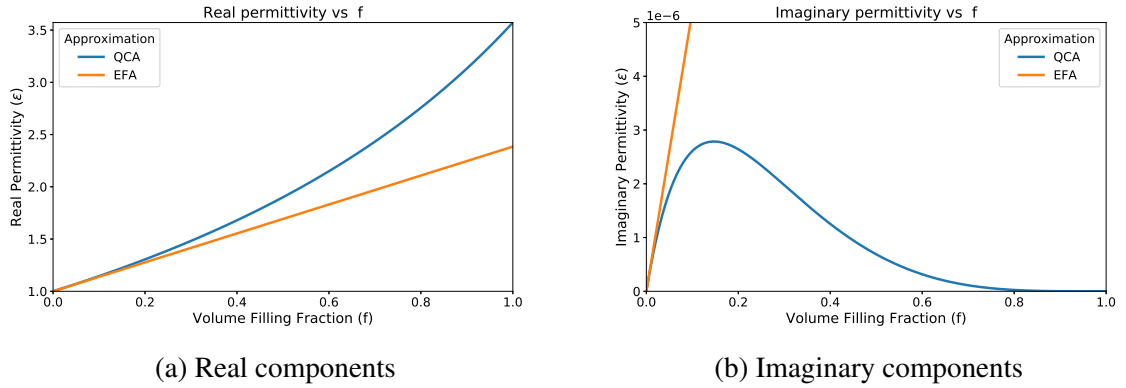


Figure 3.3: Real and complex components corresponding to each model. The nature of the expansions can be seen more clearly by viewing the behaviour of both the a) Real and b) Imaginary permittivity. Although both theories offer good agreement in the results for $f < 0.05$, there is a large divergence in the behaviour in the imaginary component which may lead to drastically different results.

In these graphs it's clearly visible that EFA is a first order approximation of the permittivity given that it appears to be a straight line tangential to the QCA approximation at small values of the volume fraction. Although the results given by QCA appear to be physically consistent, it has the disadvantage that it usually overestimates the particle radius. This usually isn't a problem but given that these approximations depend on the low frequency approximation it is assumed that $ka \ll 1$. Usually this can hold for values around 0.2 since the

term is raised to the cube but in some situations the overestimation breaks the low frequency assumption which might result in some unreliable predictions.

Chapter 4

Materials and Methods

In this section the materials used for the preparation of both the samples and the construction of the biosensor are presented. The resolution and range of the angular measurements are shown as well along with the following data processing needed to extract the numerical results from the measurements.

4.0.1 Sample preparation

Eight gold nanolayers of unknown thicknesses were acquired for the purposes of this experiment; one was left as a control layer for the calibration of our sensor and determination of the thickness. The preparation method for the Thiols, BSA and CBZ conjugates was done in accordance to the quenching methods presented in [34]; after this preparation, 6 of the remaining gold layers had different time exposure to the BSA solution (0s, 30s, 60s, 90s, 120s) while the other two gold layers were exposed for 30 seconds to the BSA-CBZ conjugate solution.

4.0.2 Experimental array

In order to generate the plasmons, the Kretschmann configuration shown in Fig. 4.1 was utilized with a HeNe 633nm 5mW polarized laser from Thorlabs given the requirement of TM polarized light in order to generate the plasmons. 3 silver coated mirrors (PF10-03-P01) were used for the correct alignment of the laser with the axis of symmetry of the cylindrical prism. The functionalized gold nanolayer was then attached to the flat side of the prism utilizing an refractive index matching oil; this prism was then mounted onto a dual stepper motor which allowed for greater control over the measurement conditions like range of the angular sweep, angular step and angular velocity. With this the data was then sent to a computer and exported as a .txt file for its subsequent analysis.

The measurements were done by doing an intensity sweep in angles between 30 and 70 with steps of 0.1° , the measurements were repeated 5 times for each layer with the results being averaged to account for the slight variations in intensity due to ambient noise. Afterwards, the same steps were repeated for the rest of the prepared samples in the same manner while making sure to wash the prism with acetone between measurements in order to prevent cross contamination. Once the data was obtained and averaged this was then processed in Python

for visualization purposes and the curve fitting via the Gradient Descent method; first, this method was programmed in order to adjust the model to the control layer. Afterwards, the third layer parameters (real refractive index, imaginary refractive index and layer thickness) were estimated for each deposition time of BSA and CBZ such that the R^2 parameter is maximized. The gradient descent model was evaluated 1000 times for each averaged measured signal to generate a 95 % confidence interval for the calculated values which are equal to 3 standard deviations from the mean. With the obtained values, the EFA and QCA dispersion relations are then used to calculate the volume filling fraction f and the particle radius a . An additional procedure is done using Eq. 3.17 in order to calculate the normalized surface coverage fraction which gives a quantitative value of the area covered by the substance.

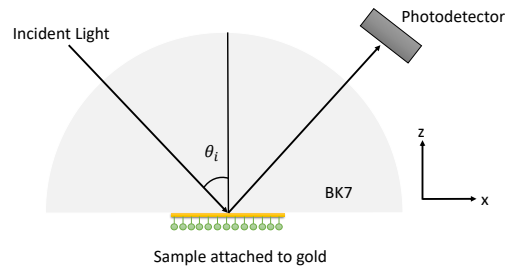


Figure 4.1: Experimental Kretschmann configuration with 4 layers. We have the BK7 prism as the first semi-infinite media; afterwards, the gold and the sample before reaching the semi-infinite air media. Light is picked up by the Photodetector which then sends the data to the computer to be analyzed later.

Chapter 5

Results

By taking the measurements of the BK7-Gold-Air system and using Gradient Descent the optimum gold thickness was determined in order to calibrate the system to the acquired gold chips. These results can be visualized in Fig. 5.1 where the analytical model is compared to the real measurements from our sensor in the range of 43 degrees to 48 degrees.

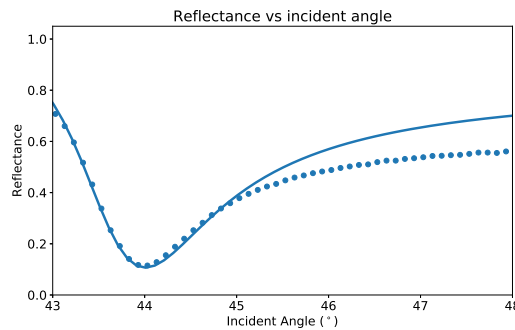


Figure 5.1: The experimental measurements (blue dots) plotted against the TMM model (blue line). The thickness of $38 \pm 0.12\text{nm}$ minimizes error function of the model with respect to the measurements and shows a good agreement with the experimental peak location.

Afterwards; the same gradient descent method was applied to the measurements made to the other gold sensors that were deposited different times in the BSA conjugate. For these cases the R^2 value or normalized MSE was used in order to determine the goodness of fit of the model. The experimental measurement of those layers can be visualized with their respective model fit in Fig 5.2b with the estimated parameters shown in Table 5.1.

With this in mind the two scattering models are now used to calculate the particle's effective radius with respect to time; first the measured refractive index is squared in order to convert it to permittivity and then the parameter values are introduced into the equations shown in Section 3.1.2 which yielded the volume filling fraction (f), normalized surface coverage (Ω_N) and the particle radius (a) in Table 5.2. Of these values only the normalized surface coverage calculated with Eq. 3.17 and the particle radius are visualized in Figures 5.3a and 5.3b respectively. Finally; the fitting process was repeated for the BSA-CBZ measurement

which can be seen in Fig. 5.4 and Table 5.3. The estimated nanoparticle radius was found to be 0.5nm for EFA and 19.5nm for QCA.

Time(s)	n_r (RIU)	n_i (RIU)	d (nm)	R^2
0	$1.0003 \pm 5.35e-4$	$(3.499 \pm 8.312)e-11$	0.025 ± 0.03	$0.999 \pm 6.3e-4$
30	$1.0597 \pm 3.05e-4$	$(1.143 \pm 0.314)e-5$	35.11 ± 0.29	$0.995 \pm 9.4e-4$
60	$1.0716 \pm 2.13e-3$	$(2.625 \pm 0.429)e-5$	35.13 ± 0.49	$0.986 \pm 7.5e-3$
90	$1.0890 \pm 8.69e-4$	$(2.041 \pm 0.623)e-5$	35.10 ± 0.37	$0.976 \pm 5.6e-3$
120	$1.0955 \pm 8.32e-4$	$(2.053 \pm 0.443)e-5$	35.18 ± 0.33	$0.954 \pm 8.9e-3$

Table 5.1: Estimated parameters of the Thiol-BSA Effective Medium using the TMM model by assuming a BK7-Gold-Sample-Air system. The estimated parameters of the sample are the real refractive index n_r , the imaginary refractive index n_i , the layer thickness d and the fitness score of the model R^2

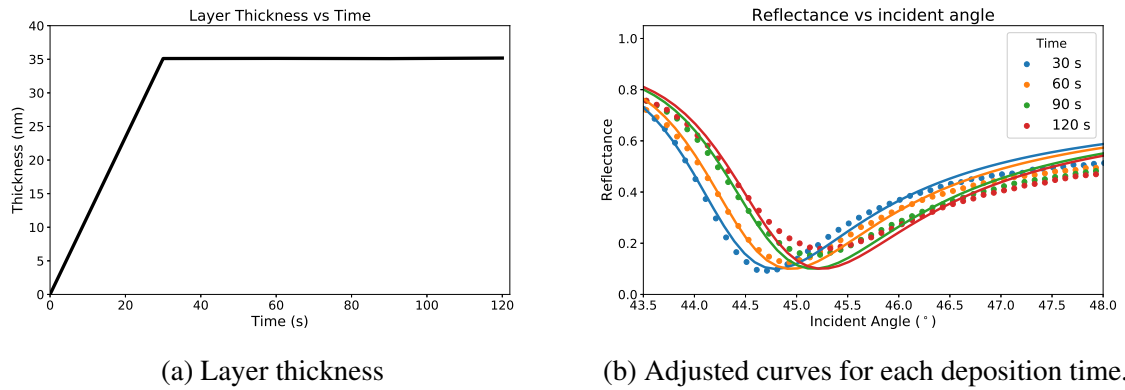


Figure 5.2: a) Effective Medium's thickness over time. b) Adjustment of the TMM model of 4 layers to each measurement done.

Time(s)	f-EFA	f-QCA	Ω_N -EFA	Ω_N -QCA	a-EFA (nm)	a-QCA(nm)
0	$0.14 \pm 1.29e-3$	$0.28 \pm 7.27e-3$	$0.27 \pm 5.21e-3$	$0.55 \pm 2.82e-2$	0.008 ± 0.003	2.57 ± 1.31
30	$8.89 \pm 5.83e-2$	$17.36 \pm 8.15e-2$	$16.99 \pm 9.09e-2$	$33.18 \pm 1.39e-1$	0.251 ± 0.077	10.33 ± 0.74
60	$10.71 \pm 1.32e-1$	$20.81 \pm 4.17e-1$	$20.48 \pm 2.88e-1$	$39.77 \pm 5.51e-1$	0.413 ± 0.053	13.93 ± 0.82
90	$13.42 \pm 1.51e-1$	$25.86 \pm 4.74e-1$	$25.65 \pm 2.95e-1$	$49.38 \pm 5.62e-1$	0.328 ± 0.085	13.45 ± 0.95
120	$14.37 \pm 1.09e-1$	$27.58 \pm 3.28e-1$	$27.46 \pm 2.74e-1$	$52.70 \pm 5.37e-1$	0.371 ± 0.092	14.75 ± 0.93

Table 5.2: Estimated average parameter models for both QCA and EFA for different BSA exposure times with a 95 % confidence interval. The volume filling fraction f and the surface coverage Ω_N are shown as percentages.

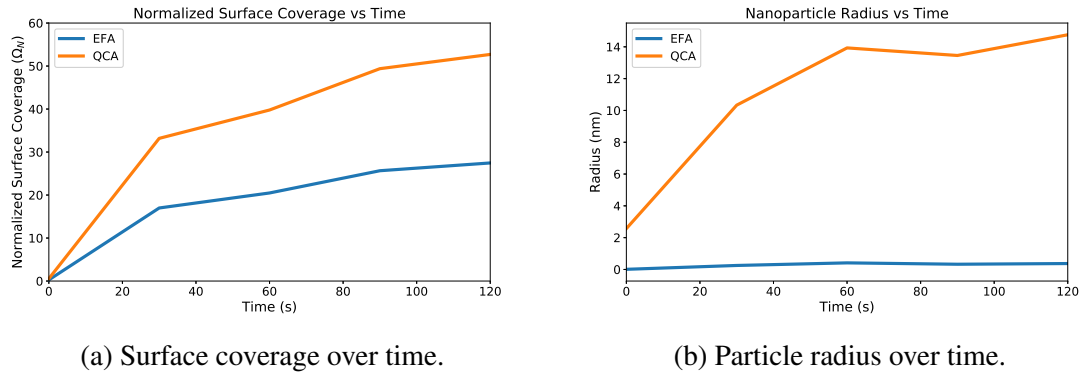


Figure 5.3: a)

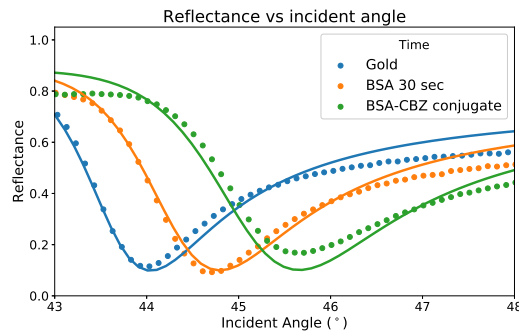


Figure 5.4: The fitted TMM model compared to the measurements of the samples immersed 30 seconds in BSA.

	n_r (RIU)	n_i (RIU)	d (nm)	R^2
BSA-CBZ	$1.117 \pm 6.56e-3$	$(4.38 \pm 1.31) e-5$	$40.79 \pm 3.72e-1$	$0.967 \pm 6.6e-3$

Table 5.3: Tabulated estimated parameters for the BSA-CBZ effective medium using the TMM model assuming a BK7-Gold-Sample-Air medium.

	f -EFA	f -QCA	Ω_N -EFA	Ω_N -QCA	a -EFA (nm)	a -QCA (nm)
BSA-CBZ	$18.01 \pm 4.45e-1$	$34.41 \pm 7.82e-1$	$34.44 \pm 5.91e-1$	$65.23 \pm 9.11e-1$	0.503 ± 0.105	19.5 ± 1.12

Table 5.4: Estimated effective medium parameters for the BSA-CBZ conjugate.

Chapter 6

Discussion

After the initial measurement of the bare gold layer for calibration purposes it was found that the gold's layer thickness is of 38nm; with this in mind the value was used for all the future measurements of both BSA and BSA-CBZ in order to remain consistent with the procedure. With respect to the different deposition times of BSA it can be seen in Table 5.1 that the real component of the refractive index increases linearly for small times before reaching saturation at about 120s. This is an interesting result since it shows that from SPR data the optimal BSA quenching time can be obtained qualitatively since after 90 seconds there is a large decrease in the change of refractive index. This was validated by the application of the effective medium theory on these values since both theories showed the same saturation behaviour albeit with different surface coverages with QCA predicting a higher normalized surface coverage of approximately 50 % whilst EFA predicted 25 %. Another interesting result can be seen in the estimated thickness of the effective medium's layer seen in Fig. 5.2a which starts close to zero and converges quickly to 35nm. This result validates the desired attachment of the BSA to the Thiols as well as the formation of a monolayer.

The complex refractive index behaviour follows a similar behaviour compared to the layer thickness; although variations do occur along time the radius still remains in the same order of magnitude which indicates that the detection of these complex components don't correspond to numerical errors. By observing the behaviour of the BSA nanoparticles in Fig. 5.3b it can be seen that the radii converges to 13nm for the QCA approximation which is a valid size for a polymer yet the EFA yields values in the Angstrom scale which is far too small for a complex molecule. There are however certain issues with this approximation since according to literature BSA corresponds to a spheroid particle with dimensions $a = 7\text{nm}$ and $b = 2.1\text{nm}$ [35] which corresponds to a sphere of mean radius of 3.1nm. Given the large difference between theoretical and experimental results it can be seen that perhaps the second order approximation might not be enough in order to estimate the radius effectively in this SPR biosensor.

After the characterization of the surface deposition of BSA the sensing the results from the BSA-CBZ measurements were analyzed. What was seen here is that there is a change in both the real component of the refractive index denoted by an increase and an increase in the medium's thickness. As it can be seen in Fig. 5.4 the individual signals of Gold, BSA and the

BSA-CBZ conjugate can be differentiated both in the experimental data and the fitted model which indicates that SPR biosensing can be used to determine the presence of CBZ in the surface but it's not associated to a specific concentration and it's detection limit doesn't allow for the resolution needed for freshwater applications since this sample has a concentration in the $\mu\text{g}/\text{L}^{-1}$ range.

Chapter 7

Conclusions and Future work

7.1 Conclusions

In conclusion a functionalized SPR biosensor capable of detecting Carbamazepine was built; by building the experimental Kretschmann configuration Fig. 4.1 and the experimental array shown in the Materials and Methods section, one is able to detect the presence of CBZ yet by processing said measurements with the analytical effective medium theory one can obtain a quantitative description of the functionalized chip to further optimize the preparation process. Out of the two scattering models used it's clear that QCA outperforms EFA in terms of better representing the physics in the sensor by estimating physically consistent nanoparticle sizes so although the estimated effective radius is several times bigger than the real values; this is a more plausible solution when compared to the Angstrom sized particles predicted by EFA.

7.2 Future work

As a next step one could apply the coherent potential theory in order to further improve the nanoparticle size approximation; since the coherent potential considers that the medium's refractive index does change as more material is added, this might result in a more complete model without modifying explicitly the hierarchy of equations. A downside to this is that the dispersion relation will have an analytical yet non-linear form which will have to be solved by the use of computational methods.

Regarding the sensing of CBZ, the current design is only able to give a qualitative detection (yes or no answer). In the future a model relating the concentration of CBZ with the sensor response should be obtained in order to be able to use the sensor in real applications.

Bibliography

- [1] L. Rayleigh, "On the Dynamical Theory of Gratings," *Proceedings of the Royal Society A: Mathematical, Physical and Engineering Sciences*, vol. 79, no. 532, pp. 399–416, aug 1907. [Online]. Available: <http://rspa.royalsocietypublishing.org/cgi/doi/10.1098/rspa.1907.0051>
- [2] R. Wood, "XXVII. *Diffraction gratings with controlled groove form and abnormal distribution of intensity*," *The London, Edinburgh, and Dublin Philosophical Magazine and Journal of Science*, vol. 23, no. 134, pp. 310–317, feb 1912. [Online]. Available: <https://www.tandfonline.com/doi/full/10.1080/14786440208637224>
- [3] E. Kretschmann and H. Raether, "Radiative Decay of Non Radiative Surface Plasmons Excited by Light," Tech. Rep., 1968. [Online]. Available: http://zfn.mpg.de/data/Reihe{_}A/23/ZNA-1968-23a-2135{_}n.pdf
- [4] A. Nooke, U. Beck, A. Hertwig, A. Krause, H. Krüger, V. Lohse, D. Negendank, and J. Steinbach, "Sensors and Actuators B : Chemical On the application of gold based SPR sensors for the detection of hazardous gases," *Sensors & Actuators: B. Chemical*, vol. 149, no. 1, pp. 194–198, 2010. [Online]. Available: <http://dx.doi.org/10.1016/j.snb.2010.05.061>
- [5] A. Amirjani and D. H. Fatmehsari, "Colorimetric detection of ammonia using smartphones based on localized surface plasmon resonance of silver nanoparticles," *Talanta*, vol. 176, no. April 2017, pp. 242–246, 2018. [Online]. Available: <http://dx.doi.org/10.1016/j.talanta.2017.08.022>
- [6] J. B. Maurya, Y. K. Prajapati, S. Raikwar, and J. P. Saini, "Optik Short note A silicon-black phosphorous based surface plasmon resonance sensor for the detection of NO₂ gas," *Optik - International Journal for Light and Electron Optics*, vol. 160, pp. 428–433, 2018. [Online]. Available: <http://dx.doi.org/10.1016/j.ijleo.2018.02.002>
- [7] A. Paliwal, A. Sharma, M. Tomar, and V. Gupta, "Carbon monoxide (CO) optical gas sensor based on ZnO thin films," *Sensors & Actuators: B. Chemical*, no. 250, pp. 679–685, 2017. [Online]. Available: <http://dx.doi.org/10.1016/j.snb.2017.05.064>
- [8] O. Tokel, U. H. Yildiz, F. Inci, N. G. Durmus, O. O. Ekiz, B. Turker, C. Cetin, S. Rao, K. Sridhar, N. Natarajan, H. Shafiee, A. Dana, and U. Demirci, "Portable Microfluidic Integrated Plasmonic Platform for Pathogen," *Scientific Reports*, pp. 1–9, 2015.

- [9] A. S. Kushwaha, A. Kumar, R. Kumar, and M. Srivastava, "Optik Zinc oxide , gold and graphene-based surface plasmon resonance (SPR) biosensor for detection of pseudomonas like bacteria : A comparative study," *Optik - International Journal for Light and Electron Optics*, vol. 172, no. March, pp. 697–707, 2018. [Online]. Available: <https://doi.org/10.1016/j.ijleo.2018.07.066>
- [10] E. Makhneva, P. Skl, and L. Zaj, "Cyclopropylamine plasma polymer surfaces for label free SPR and QCM immunosensing of Salmonella(Accepted Manuscript)," *Sensors and Actuators B*, 2018.
- [11] L. Song, L. Zhang, Y. Huang, L. Chen, G. Zhang, Z. Shen, J. Zhang, Z. Xiao, and T. Chen, "Amplifying the signal of localized surface plasmon resonance sensing for the sensitive detection of Escherichia coli O157:H7," *Scientific Reports*, vol. 7, no. 1, p. 3288, 2017. [Online]. Available: <http://www.nature.com/articles/s41598-017-03495-1>
- [12] A. Razmi, A. Golestanipour, M. Nikkhah, A. Bagheri, M. Shamsbakhsh, and S. Malekzadeh-Shafaroudi, "Localized surface plasmon resonance biosensing of tomato yellow leaf curl virus," *Journal of Virological Methods*, vol. 267, no. February, pp. 1–7, 2019. [Online]. Available: <https://doi.org/10.1016/j.jviromet.2019.02.004>
- [13] B. Osman, A. Denizli, B. Osman, A. Denizli, M. Imprinted, and S. Plasmon, "Molecularly Imprinted Surface Plasmon Resonance (SPR) Sensor for Uric Acid Determination," *Sensors and Actuators*, 2017.
- [14] M. Morsin, M. M. Salleh, A. A. Umar, and M. Z. Sahdan, "Gold nanoplates for a localized surface plasmon resonance-based boric acid sensor," *Sensors (Switzerland)*, vol. 17, no. 5, pp. 1–10, 2017.
- [15] Y. Takimoto, A. Monkawa, K. Nagata, and M. Kobayashi, "Detection of SO₂ at the ppm Level with Localized Surface Plasmon Resonance (LSPR) Sensing," *Plasmonics*, no. 15, pp. 805–811, 2019.
- [16] P. Zhang, Y.-p. Chen, W. Wang, Y. Shen, and J.-s. Guo, "Trends in Analytical Chemistry Surface plasmon resonance for water pollutant detection and water process analysis," *Trends in Analytical Chemistry*, vol. 85, pp. 153–165, 2016. [Online]. Available: <http://dx.doi.org/10.1016/j.trac.2016.09.003>
- [17] Y. Erkut, N. Bereli, D. Türkmen, and A. Denizli, "Plastic antibody based surface plasmon resonance nanosensors for selective atrazine detection," *Materials Science and Engineering C*, vol. 73, pp. 603–610, 2017.
- [18] L. H. M. L. M. Santos, A. N. Araújo, A. Fachini, A. Pena, C. Delerue-matos, and M. C. B. S. M. Montenegro, "Ecotoxicological aspects related to the presence of pharmaceuticals in the aquatic environment," *Journal of Hazardous materials*, vol. 175, pp. 45–95, 2010.
- [19] J. C. Alvarez, B. Prado, D. González, Y. Sánchez, and B. Jiménez-cisneros, "Environmental fate of naproxen , carbamazepine and triclosan in wastewater , surface

- water and wastewater irrigated soil — Results of laboratory scale experiments,” *Science of the Total Environment*, vol. 538, pp. 350–362, 2015. [Online]. Available: <http://dx.doi.org/10.1016/j.scitotenv.2015.08.028>
- [20] S. Ortiz, D. García, G. Pinto, P. A. García-encina, and R. Irusta, “Ranking of concern , based on environmental indexes , for pharmaceutical and personal care products : An application to the Spanish case,” *Journal of Environmental Management*, vol. 129, pp. 384–397, 2013. [Online]. Available: <http://dx.doi.org/10.1016/j.jenvman.2013.06.035>
- [21] D. J. Griffiths, *Introduction to Electrodynamics*, 4th ed. Cambridge University Press, 2017.
- [22] M. Dressel, M. Scheffler, and P. Institut, “Verifying the Drude response,” *Annalen Der Physik*, vol. 544, no. 7, pp. 535–544, 2006.
- [23] S. D. Elia, N. Scaramuzza, F. Ciuchi, C. Versace, G. Strangi, and R. Bartolino, “Applied Surface Science Ellipsometry investigation of the effects of annealing temperature on the optical properties of indium tin oxide thin films studied by Drude – Lorentz model,” *Applied Surface Science*, vol. 255, no. 16, pp. 7203–7211, 2009.
- [24] S. a. Maier, *Fundamentals and Applications Plasmonics : Fundamentals and Applications*. Springer, 2004, vol. 677, no. 1. [Online]. Available: <http://elib.tu-darmstadt.de/tocs/95069577.pdf>
- [25] D. Barchiesi and T. Grosjes, “Fitting the optical constants of gold , silver , chromium , titanium , and aluminum in the visible bandwidth,” *Journal of Nanophotonics*, vol. 8, 2014.
- [26] C. C. Katsidis and D. I. Siapkas, “General transfer-matrix method for optical multi-layer systems with coherent, partially coherent and incoherent sources,” *Applied Optics*, vol. 41, no. 19, pp. 3978–3987, 2002.
- [27] G. Hecht, *Optics*, 5th ed. Pearson, 2016.
- [28] L. Novotny and B. Hecht, *Principles of Nano-Optics*, 2nd ed. New York: Cambridge University Press, 2012.
- [29] K. Takagi, S. V. Nair, R. Watanabe, and K. Seto, “Surface Plasmon Polariton Resonance of Gold , Silver , and Copper Studied in the Kretschmann Geometry : Dependence on Wavelength , Angle of Incidence , and Film Thickness,” *Journal of the Physical Society of Japan*, vol. 86, pp. 1–11, 2017.
- [30] S. Nocedal, Jorge; Wright, *Numerical Optimization*, 2nd ed. Springer, 2006.
- [31] S. Salsa, *Partial Differential Equations in Action*, 2nd ed. Springer, 2008.
- [32] L. Tsang and J. A. Kong, “Multiple scattering of electromagnetic waves by random distributions of discrete scatterers with coherent potential and quantum mechanical formalism Multiple scattering of electromagnetic waves by random distributions of discrete scatterers with coherent,” *Journal of Applied Physics*, vol. 51, no. 7, 1980.

- [33] J. Tsang, Leung; Kong, *Scattering of Electromagnetic Waves Advanced Topics*, 1st ed. John Wiley & Sons, 2001.
- [34] C. W. Ang, Z. W. Ang, and J. Z. Hao, "Study of the Interaction of Carbamazepine with Bovine Serum Albumin by Fluorescence Quenching Method," *Analytical Sciences*, vol. 22, no. March, 2006.
- [35] A. K. Wright and M. R. Thompson, "Hydrodynamic structure of Bovine Serum Albumin determined by Transient Electric Birefringence," *Biophysical Journal*, vol. 15, no. 2, pp. 137–141, 1975. [Online]. Available: [http://dx.doi.org/10.1016/S0006-3495\(75\)85797-3](http://dx.doi.org/10.1016/S0006-3495(75)85797-3)

Curriculum Vitae

Alejandro Balderas Elizalde was born in Monterrey, México, on November 30, 1994. He earned the Engineering Physics degree from the Instituto Tecnológico y de Estudios Superiores de Monterrey, Monterrey Campus in May 2008. He was accepted in the graduate programs in Nanotechnology in May 2018.

This document was typed in using L^AT_EX 2_ε^a by Alejandro Balderas Elizalde.

^aThe style file `phdThesisFormat.sty` used to set up this thesis was prepared by the Center of Intelligent Systems of the Instituto Tecnológico y de Estudios Superiores de Monterrey, Monterrey Campus